Astronomy & Astrophysics manuscript no. output
October 28, 2021

Modeling the Mg I from the NUV to MIR: I. The solar case

J. I. Peralta[1,2], M. C. Vieytes[1,2], A. M. P. Mendez[1], and D. M. Mitnik[1,3]

[1] Instituto de Astronomía y Física del Espacio, CONICET–Universidad de Buenos Aires, Argentina
e-mail: jperalta@iafe.uba.ar; mariela@iafe.uba.ar
[2] Departamento de Ciencia y Tecnología, UNTREF, Argentina
[3] Departamento de Física, Universidad de Buenos Aires, Argentina

Received 6 August 2021, Accepted 6 October 2021

ABSTRACT

Context. Semi-empirical models of the solar atmosphere are used to study the radiative environment of any planet in our Solar System. There is a need for reliable atomic data for neutral atoms and ions in the atmosphere to obtain improved calculated spectra. Atomic parameters are crucial to computing the correct population of elements through the whole stellar atmosphere. Although there is very good agreement between the observed and calculated spectra for the Sun, there is still a mismatch in several spectral ranges due to the lack of atomic data and the inaccuracies thereof, particularly for neutrals such as Mg I.
Aims. To represent many spectral lines of Mg I from the near-ultraviolet to the mid-infrared correctly, it is necessary to add and update the atomic data involved in the atomic processes that drive their formation.
Methods. The improvements made to the Mg I atomic model are as follows: *i)* 127 strong lines, including their broadening data, were added. *ii)* To obtain these new lines, we increased the number of energy levels from 26 to 85. *iii)* Photoionization cross-section parameters were added and updated. *iv)* Effective collision strength (Υ_{ij}) parameters were updated for the first 25 levels using the existing data from the convergent close-coupling (CCC) calculations. One of the most significant changes in our model is given by the new Υ_{ij} parameters for transitions involving levels between 26 and 54, which were computed with a multiconfiguration Breit–Pauli distorted–wave (DW) method. For transitions involving superlevels, we calculated the Υ_{ij} parameters with the usual semi-empirical formulas of Seaton (1962) and van Regemorter (1962).
Results. More than 100 transitions were added to our calculations, increasing our capability of reproducing important features observed in the solar spectra. We found a remarkable improvement in matching the solar spectra for wavelengths higher than 30 000 Å when our new DW Υ_{ij} data were used in the model.
Conclusions.

Key words. atomic:data – sun:atmospheres – Sun:infrared – line:formation – line:profile

1. Introduction

The 1D semi-empirical model calculation of the solar atmosphere continues to be useful to predict and reproduce the solar spectral irradiance (SSI), from the far-infrared (FIR) to the extreme ultraviolet (EUV), received at the top of Earth's atmosphere (Fontenla & Landi 2018). Changes in the SSI can produce modifications in the chemistry of our atmosphere.

The advantage of these models is that they are built to reproduce a large number of observations in different wavelengths. The equations of statistical equilibrium and radiative transfer are treated in detail and solved simultaneously for all the species in the atmosphere. The most critical parameters are the data describing the atomic and molecular species present in the atmosphere. Great efforts have been made to obtain experimental and theoretical data. However, there is still a lack of complete and accurate atomic data, particularly for neutral and low ionized atoms. These atomic species, such as Mg I, are of particular interest because they have relevant spectral features used in the diagnosis of solar and stellar astrophysics. The influence of using a more complete and accurate atomic model for neutral atoms in SSI calculations can be found, for example, in Vieytes & Fontenla (2013), were the improvements made in the Ni I atomic model led to a better match with observations, mainly in the near-ultraviolet (NUV) region.

Neutral magnesium is an important chemical element since its lines are strong in the spectra of late-type and even in metal-poor stars, making it a good tracer of α-element abundances. At chromospheric temperatures, magnesium is susceptible to deviations from local thermodynamic equilibrium (LTE). These deviations from LTE are predicted to be significant, particularly for metal-poor stars (Zhao et al. 1998; Zhao & Gehren 2000). Therefore, in order to study the non-LTE (NLTE) effects, it is necessary to account for accurate atomic data.

Past studies have used semi-empirical formulae when computing electron atomic collision data. The most widely used semi-classical formulas for radiative-allowed transitions are the ones given by Seaton (1962) and van Regemorter (1962) since they provide estimates for the collision rates based on the oscillator strengths and transition energies. However, these approximations can lead to a great number of uncertainties in the synthetic spectra of NLTE atmospheric models, such as spectral lines in emission instead of in absorption as observations reveal.

There are several studies on NLTE calculations of Mg I in the Sun and other stars, for instance, the recent works by Alexeeva et al. (2018), the paper series by Osorio et al. (2015), Osorio & Barklem (2016), and Barklem et al. (2017), and the relevant works by Bergemann et al. (2015) and Scott et al. (2015). In all of these studies, the authors stress the need for accurate Mg I atomic data.

Osorio et al. (2015) describe, in detail, previous studies of NLTE Mg I line formation. They present a complete Mg I atomic model of 108 energetic states, including fine-structure splitting, up to the level 20*d*. Among other important improvements, they included new electron impact values for low-lying states using the R-Matrix method. For transitions involving states greater than $5p\,^3$P, the data are complemented with the Seaton (1962) formula. The authors analyze relevant spectral lines from ~3800 Å to ~8800 Å, including the following mid-IR (MIR) lines: 7.3, 12.2, 12.3, 18.8, and 18.96 μm. The NLTE calculation was computed using the *MULTI* code (Carlsson 1992). Their synthetic spectra showed good agreement with solar observations and with observations of five F-G-K late-type stars with reliable fundamental parameters. Barklem et al. (2017) presented the latest calculations for inelastic e+Mg for the first 25 energy states of neutral magnesium (up to $3s6p\,^1P$), produced by the convergent close-coupling (CCC) and the B-spline R-matrix (BSR) methods. In this work, the authors suggest their CCC data for NLTE modeling.

Later, Alexeeva et al. (2018) carried out an extensive study of NLTE Mg I line formation in the Sun and 17 stars, covering B-A-F-G-K spectral types. They used an atomic model of about 89 energetic states, up to level $n = 16$. For electronic collisions, they implemented data from Osorio et al. (2015) and complemented them with data from the Seaton (1962) formula for allowed transitions. In the case of forbidden transitions, the authors assumed a single value for the effective collision strength, being $\Upsilon_{ij} = 1$. To test their results, they also selected spectral lines starting at ~3800 Å until ~8800 Å, and included the following MIR lines: 7.3, 12.2, and 12.3 μm. The NLTE calculation was made using the *DETAIL* code (Butler & Giddings 1985).

None of the previous works on Mg I line formation reproduced spectral lines in the NUV region or lines between ~8800 Å and 7.3 μm in the NIR and MIR. Nevertheless, the NUV plays a fundamental role in ozone formation, and any calculation of the SSI must reproduce this region as well as possible.

Everything we know about our Sun and its relationship with Earth's atmosphere can be extended and applied to study the atmosphere of exoplanets orbiting around late-type stars. The same methodology can be used to calculate the spectral energy distribution (SED) that an exoplanet orbiting a late-type star receives at the top of its atmosphere (Tilipman et al. 2021).

Nonetheless, our Sun can be observed with unique spatial and spectral resolution. For this reason, changes in the atomic models included in the atmospheric modeling must first be tested to reproduce the observed solar spectra.

The goal of the present work is two-fold. We intend to update the Mg I atomic model. Consequently, we expect to extend the analysis of spectral line formation of Mg I to include transitions in a broader range than previous studies, from the NUV (1700 Å) to MIR (72 000 Å).

Regarding the electronic collisions, we included two significant improvements to the electron impact excitation data. From our original atomic model, we replaced the semi-empirical effective collision strength (Υ_{ij}) values for the first 25 lower-lying terms by close-coupling calculations (Barklem et al. 2017). Furthermore, we used the AUTOSTRUCTURE code (Badnell 2011) to calculate collisional strengths under the distorted wave approximation. We incorporated these results by replacing the semi-empirical Υ_{ij}, involving states between $3s6p$ and $3s7i$.

This paper is structured as follows: The code used in our NLTE and spectra calculations together with the initial atomic model is detailed in Section 2. Section 3 shows the different Mg I atomic models built. The observations used to compare them with our synthetic spectra are described in Section 4. Our results and discussion are presented in Section 5, while our final remarks and conclusions are provided in Section 6.

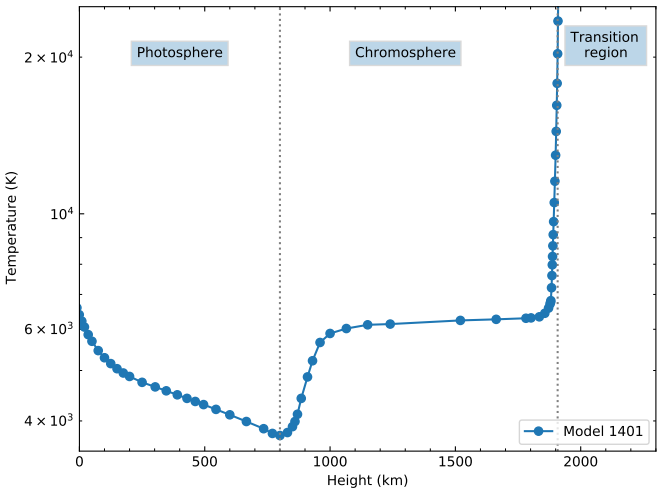

Fig. 1. Atmospheric model 1401 by Fontenla et al. (2015). Models in this work have the same thermal structure as 1401.

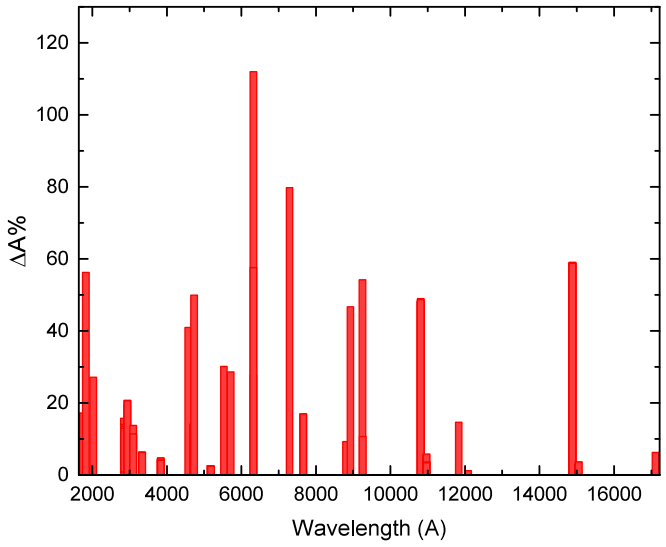

Fig. 2. Distribution of changes between the original and the updated *A* coefficients for wavelengths included in model 1401a.

2. NLTE and initial emergent spectra calculations

2.1. SRPM system and the solar model employed

We carried out the NLTE and spectra calculations by making use of the *Solar Radiation Physical Modeling (SRPM)* version 2 system; the first version was developed by Fontenla & Harder (2005), and it was later updated by Fontenla et al. (2015). This system is a library of codes that allows us to calculate the equations of statistical equilibrium and radiative transfer self-consistently for a plane-parallel or spherical symmetric atmosphere, assuming hydrostatic equilibrium.

One key point of the *SRPM* system is that it computes full NLTE for all atomic species in the atmosphere based on the net radiative bracket operator formulation implemented by Fontenla

Table 1. Atomic models summary.

Model	Mg I levs	Mg II levs	Υ_{ij} methods (Mg I)	Details
1401	26	14	SEA&VRM	Original model in Fontenla et al. (2015)
1401a	26	14	SEA&VRM	*gf* and broad. data updated
1401b	85	47	CCC (< lev 26) + SEA&VRM (levs 26 to 85)	*gf*, broad. and photoioniz. data updated
1401c	85	47	CCC (< lev 26) + DW (levs 26 to 54) + SEA&VRM (levs 55 to 85)	*gf*, broad. and photoioniz. data updated

Notes. The atmospheric structure of model 1401 (Fontenla et al. 2015) was used in each model built.

& Rovira (1985). This method was further developed to include Partial ReDistribution (PRD) (Fontenla et al. 1996), particle diffusion, and flows, as outlined by Fontenla et al. (1990) and Fontenla et al. (1991).

The *SRPM* calculates the populations of H, H^-, and H_2 as well as 52 neutral and lowly ionized atomic species (see Table 2 in Fontenla et al. (2015)) in optically thick full NLTE and PRD. Additionally, the optically thin NLTE approximation is used for 198 highly ionized species. Our atomic database takes into account 18 538 levels and 435 986 transitions produced by atoms and ions. Apart from atomic species, the 20 most abundant diatomic molecules and over 2 million molecular lines are included.

The *SRPM* has been widely used to build models for each different feature observed on the solar disk, and then successfully tested against ground- and space-based solar spectra. These models can accurately reproduce observations of the SSI, including the UV region observed by a number of space missions with good absolute flux calibration (see Fontenla & Landi (2018) and references therein for more detail).

The solar atmospheric model used to calculate the NLTE populations and the solar spectra for the different sets of Mg I atomic models is the model 1401 built by Fontenla et al. (2015), which is presented in Fig. 1. This model reproduces the quiet sun inter-network (see Table 1 in that paper), and represents the different layers of the solar atmosphere, the photosphere, the chromosphere, and the transition region, as shown in Fig. 1. Considering solar disk observations in the minimum of the activity cycle, the quiet sun inter-network is the dominant feature on the disk when a multicomponent model for the atmosphere of the quiet Sun is calculated.

2.2. Initial atomic model

In this section, we describe the initial atomic models for the neutral and the first two ionized atoms, Mg I, Mg II, and Mg III. These atomic models constitute the starting model 1401. The population of these species was calculated in full NLTE. It is important to note that we also considered the rest of the ionization states in optically thin NLTE, and they were taken into account for the ionization balance of the Mg atomic element.

Mg I. The original atomic model was developed by Fontenla et al. (2006) with data from *NIST*[1] (Kramida et al. 2004). This model included 26 energy levels (up to $3s5g\ ^3G$, 57 262.76 cm^{-1}) with their fine-structure splitting, which produce a total of 44 energy sublevels[2]. This model included 82 Mg I spectral lines in the range of 1700–18 000 Å. The Υ_{ij} parameters for excitation due to the collision with electrons were obtained from the semi-empirical equations of Seaton (1962) (hereafter SEA) for allowed transitions and van Regemorter (1962) (hereafter VRM) when transitions were forbidden. For ionizing collisions, the NRL Plasma Formulary (2005) ionization rate equation was used. Photoionization cross sections were taken from *TOPbase*[3] the Opacity Project atomic database (Cunto et al. 1993). Also, Mg I data included cross sections up to level $3s5g\ ^{1,3}G$ (level 26 in our database). The radiative recombination is included as the inverse of the photoionization process. We also considered the dielectronic recombination for the ionization balance, but only for the ground state of the species. These values were taken from *CHIANTI* version 7.1 (Landi et al. 2012). For the line broadening parameters concerning radiative, Stark, and van der Waals processes, the approximate values by Kurucz & Bell (1995) were used.

Mg II. The atomic model included 14 levels (up to $6p\ ^2P$, 105 622.34 cm^{-1}), with a total of 23 energy states considering the fine-structure splitting. With this structure, 52 line transitions were included (22 for term-term transitions) in the range of 1020–11 000 Å. The Υ_{ij} data were extracted from the *CHIANTI*[4] atomic database (versions 5.2 and 7.1) and complemented with SEA (allowed transitions) and VRM (forbidden transitions) when missing in *CHIANTI*. For ionizing collisions, the NRL equation was used. Furthermoer, Mg II photoionization cross-section data were taken from *TOPbase*. Radiative and dielectronic recombination were considered as in Mg I.

Mg III. The model included 54 energy levels (up to $2s^2\,2p^5\,[^2P_{3/2}]\,6d$, 618 601 cm^{-1}) and 346 spectral lines (141 term-term transitions). For Υ_{ij} parameters, the SEA&VRM combination was used. Also, Mg III photoionization cross-section parameters from *TOPbase* for all levels in the database are included. Radiative and dielectronic recombination were considered as in the previous ions. The Mg III atomic model remains unchanged throughout this work.

3. The set of new atomic models

The aim of the present work is to improve the Mg I calculated features in the solar spectra using the abovementioned atmospheric model 1401. To this end, we built a set of variants of the model 1401 with a different Mg I model, but maintaining the same temperature versus height atmospheric structure. We also modified the Mg II atomic model, but the rest of the atomic and molecular species were maintained in every variant. In this way, we were able to detect variations in the calculated spectra due

[1] https://www.nist.gov/pml/atomic-spectra-database

[2] For clarification, we follow the common nomenclature "level", to refer to the ^{2S+1}L term, and "sublevel" when referring to a fine-structure $^{2S+1}L_J$ level.

[3] http://cdsweb.u-strasbg.fr/topbase/xsections.html

[4] https://www.chiantidatabase.org/

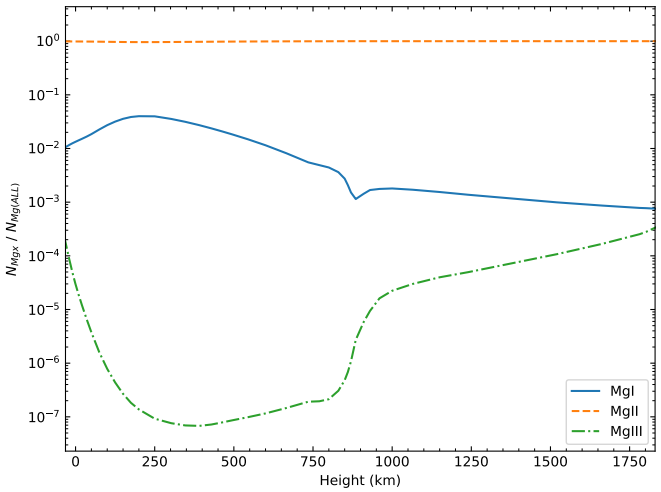

Fig. 3. Mg I (blue line), Mg II (orange dashed line), and Mg III (green dashed-dotted line) densities relative to the total magnesium density for atmospheric model 1401 as a function of height.

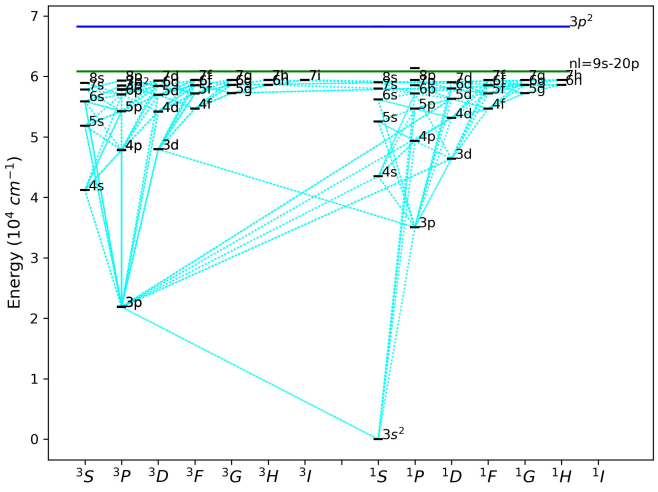

Fig. 4. Mg I Grotrian diagram for the structure of 85-level models. Fine structure is included up to level $7i\,^1I$ (level 54, 59 430.517 cm^{-1}) (not distinguishable in the figure). The first 54 energy levels are fully represented. Superlevels (between $nl = 9s$ and $20p$) are shown with their average energy as a solid green line, very close to the continuum (which occurs at 61 671.05 cm^{-1}). Level $3p^2$ (68 275 cm^{-1}) is represented as a solid blue line. In cyan dashed lines, the 210 transitions included in the spectrum are shown.

to the imposed changes to the Mg I atomic model. Table 1 lists the models built and its characteristic modifications, which are described in detail in the following.

3.1. Updating the atomic data (model 1401a)

New experiments and theoretical developments continue to provide more and new accurate atomic data. This information is continuously being updated in public databases. Consequently, atomic models must also be updated to obtain reliable spectra.

Model 1401a was built to identify the changes in the spectrum due to updated atomic data, maintaining the 26 energy levels' structure for the Mg I atomic model, and the original 82 transition lines. The update was focused on the oscillator strengths (gf), Einstein coefficients (A), and broadening parameters of the spectral lines considered. Regarding the gf and A parameters, they were obtained from *NIST* database version 5.7.1 (Kramida et al. 2020). Radiative, Stark, and van der Waals broadening parameters, initially missing from our database, were taken from the *VALD3*[5] database (Kupka et al. (2000)) and, when it was absent in *VALD3*, from the *Kurucz* database (Kurucz & Bell 1995)[6].

We updated 71 values for A in total. Figure 2 shows the distribution of changes in this parameter throughout the spectral range. The maximum change obtained was of 112% in 6 320.46 Å ($4s\,^3S_1$–$6p\,^3P_{0,1,2}$), meanwhile the minimum was of 0.8% in 2 852.96 Å ($3s^2\,^1S$–$3p\,^1P$). It is important to note that changes in the A parameter implied a re-computation of the collisional Υ_{ij} data obtained using SEA&VRM formulas. Regarding the broadening parameters, the Stark and van der Waals data were filled for 24 transitions.

3.2. Atomic structure. Including more lines (models 1401b and 1401c)

The structure of 26-energy levels in the initial Mg I atomic model (used in atmospheric model 1401 and 1401a) limits our capacity of reproducing strong lines in the NUV, and a major number of lines, higher than 17 000 Å, in the IR. In addition, the original highest energy level of 57 262.76 cm^{-1} ($3s5g\,^1G$) was very far from the next ionization state Mg II, at 61 671.05 cm^{-1}. Figure 3 shows the distribution of Mg I, Mg II, and Mg III relative to the total abundance of Mg at each height throughout the atmosphere of the model 1401; Mg II is clearly the most abundant ionization state. As the majority of the population is concentrated in the Mg II ground state, to obtain a realistic Mg I atomic model, it should be necessary to include Rydberg energy levels closely coupled with this ground state. This effect was solved in our models 1401b and 1401c by significantly increasing the amount of energy levels, coupled to the lower states of Mg II by collisional ionization and recombination processes. In what follows, we detail the new energy structure for the Mg I and Mg II atomic models used in 1401b and 1401c atmospheric models, maintaining the updates made in the previous section to the first 26 levels and corresponding transitions.

Mg I. The energy structure was built to obtain an optimized atomic model capable of including new lines with minimal computational cost. The maximum energy level was increased to $3s20p\,^1P$ (61 365.55 cm^{-1}) using values from the *NIST* database, as in the Mg I models from Osorio et al. (2015) and Alexeeva et al. (2018), although a previous version of the *NIST* database was used in these works. Levels $3p^2\,^1S$ (68 275 cm^{-1}) and $3p^2\,^3P_{0,1,2}$ (57 812.77 cm^{-1}) were also included. We incorporated the fine-structure splitting for all levels up to $3s7i\,^3I$ (59 430.517 cm^{-1}). Levels $3snl$ with $n \geq 8$ and $l \geq 2$ with the same main quantum number n were merged into one state (e.g., $8d$ to $8h$, $9d$ to $9k$, and so on). For $n \geq 9$, superlevels were also considered when $l = s, p$ to combine singlets with triplets in higher levels.

The structure of our final Mg I model was formed by 85 levels and 129 sublevels. This allows one to obtain transitions involving Rydberg states, and also population exchange from the next ionization states (Mg II, Mg III, etc). Figure 4 shows, through a Grotrian diagram, the Mg I structure of levels and sublevels. Superlevels are represented by one state as a solid green line at

[5] http://vald.astro.uu.se
[6] http://kurucz.harvard.edu/linelists/gfall/

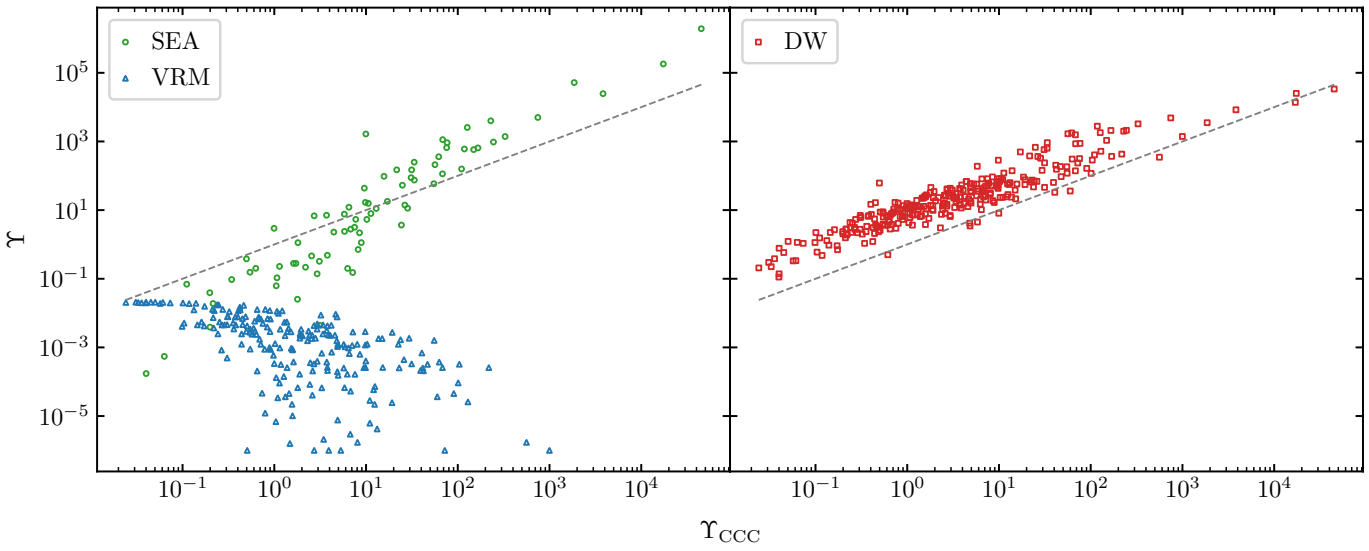

Fig. 5. Comparison of effective collision strengths Υ_{ij} at $T = 6000$ K. *Left*: CCC calculations vs. SEA (circles) and VRM (triangles) values. *Right*: CCC data vs. DW (squares) results. Lines: CCC one-to-one relation (dashed).

average energy. Singlets and triplets are separated for better visualization.

To obtain the most relevant lines missing in the old atomic model, we performed a query on the *NIST* database using the following criteria: $\log(gf) > -1$, a maximum energy level of 59 649.15 cm^{-1} ($3s9s\,^3S$), and a maximum wavelength (in vacuum) of 71 500 Å. As a result of this query, 127 lines were added to our database. This number is reduced to 58 if the distinction in quantum number J is not considered.

The Mg I photoionization cross sections that are currently available in the *TOPbase* database were used in our new 85-level model, which includes transitions with $n \leq 9$ and $l \leq 4$. Consequently, the radiative recombination coefficients considered were also modified. Concerning the broadening parameters for the new lines, 33 transitions were completed with radiative, Stark, and van der Waals parameters from *VALD3* and *Kurucz* databases. When the broadening parameters for the different possible processes for a certain transition were missing, the SRPM system solely considered the natural broadening parameter as $A_{ij}/4\pi$.

Mg II. For models 1401b and 1401c, the Mg II atomic model was also updated. The number of energy levels was expanded from 14 ($6p\,^2P$, 105 622.34 cm^{-1}) to 47 ($2p^6\,11g\,^2G$, 117 639.51 cm^{-1}) using the *NIST* database. The new structure included fine structure splitting without superlevels, resulting in a total of 90 sublevels. Consequently, we increased the number of transition lines from 52 to 781 (22 to 291 for term-term transitions), of which 405 lines were taken from the *NIST* database and the remaining are from the *Kurucz* database. We were able to compute Mg II spectral lines in the enormous range of 850–6 342 878 Å. The broadening parameters for the new lines were extracted from the *Kurucz* database, when available. The electron impact parameters Υ_{ij} for the new collisional transitions were calculated employing the SEA&VRM combination formulas. For ionizing collisions, the NRL Plasma Formulary (2005) equation was used. Finally, the photoionization (and the radiative recombination as the inverse process) data available in the *TOPbase* database were used in our new 47-level model.

Table 2. Statistical parameters.

Parameters	DW	SEA	VRM
μ^*	5.07	2.06	8.4×10^{-4}
σ^*	2.29	9.33	22.85

Notes. Geometric mean and standard deviation of the ratio $\Upsilon/\Upsilon_{\rm CCC}$ for the semi-empirical models and perturbation calculations.

3.3. *Effective collision strengths* (Υ_{ij}) *for* Mg I *in 1401b and 1401c models*

The benchmark excitation rate coefficients for Mg I are currently given by Barklem et al. (2017). The complexity of computing the electron impact excitation of neutral atoms is widely known. For close-coupling methods, it requires the inclusion of a large number of states to account for the higher Rydberg states and the coupling to the continuum. For example, the current benchmark included 712 states, of which 680 were continuum pseudo-states. Despite a large number of terms, the atomic model considered enables one to correctly compute the excitation collision strengths only between the first 25 lower-lying levels.

The spectral lines studied in this work involve transitions in the NUV and MIR, which correspond to levels higher than the $3s6s\,^1P$ term. However, there are no close-coupling calculations currently available for these levels. Since the transitions between higher levels are difficult to calculate within the close-coupling framework, we resorted to a perturbation approximation. In particular, a multi-configuration Breit-Pauli distorted-wave (DW) method was employed to compute the effective collision strength for a certain number of levels. It is well documented that perturbation techniques tend to overestimate Υ_{ij}, and this effect is even greater in neutral targets. Nonetheless, we consider that these quantum calculations could represent a significant improvement over the semi-empirical ones. The present DW results were obtained employing the AUTOSTRUCTURE code[7] using nonrelativistic radial wave functions in intermediate coupling. Theoretical details of the method can be found in Badnell (2011) and references

[7] http://amdpp.phys.strath.ac.uk/autos

Table 3. Term-term line transitions shown in this work.

λ_{vac} [a] (Å)	Transition	Transition Level Numbers L(SL)–U(SU)	log gf [a]	log Γ_4/N_e [b] ($rad\ s^{-1}\ cm^3$)	log Γ_6/N_H [b] ($rad\ s^{-1}\ cm^3$)	Fig.
2 780.6	$3p\,^3P_{0,1,2}$–$3p^2\,^3P_{0,1,2}$	2(1,2,3)–28(1,2,3)	0.749	-5.98	-7.70	9
4 572.4	$3s^2\,^1S_0$–$3p\,^3P_1$	1(1)–2(2)	-5.623	-6.89	-7.69	6
6 320.7	$4s\,^3S_1$–$6p\,^3P_{0,1,2}$	4(1)–22(1,2,3)	-1.848	-4.57	-7.10	7, 10
10 964.4	$4p\,^3P_{0,1,2}$–$5d\,^3D_{1,2,3}$	7(1,2,3)–21(1,2,3)	0.091	-3.40	-7.10	7, 10
33 200.6	$4d\,^3D_{1,2,3}$–$5f\,^3F_{2,3,4}$	13(1,2,3)–24(1,2,3)	0.953	-3.71	-7.10	11a
36 807.6	$5p\,^3P_{0,1,2}$–$5d\,^3D_{1,2,3}$	14(1,2,3)–21(1,2,3)	0.74	-3.40	-7.10	11b
38 664.9	$4f\,^1F_3$–$5g\,^1G_4$	15(1)–26(1)	0.949	-3.71	-7.10	11c
38 669.1	$4f\,^3F_{2,3,4}$–$5g\,^3G_{3,4}$	16(1,2,3)–27(1,2)	1.199	-3.71	-7.10	11c
38 670.4	$6s\,^3S_1$–$7p\,^3P_2$	18(1)–33(3)	-0.837	-3.01	-6.90	11c
71 092.0	$5f\,^1F_3$–$6g\,^1G_4$	23(1)–37(1)	0.866	-3.01	-7.00	11d
71 097.4	$5f\,^3F_{2,3,4}$–$6g\,^3G_{3,4,5}$	24(1,2,3)–38(1,2,3)	1.345	-3.01	-7.00	11d

Notes. [a] Extracted from the *NIST* database (version 5.7.1). [b] Broadening parameters from Kurucz & Bell (1995). Γ_4 and Γ_6 are given at 5 000 K.

therein. For models 1401b and 1401c, the electronic structure considered includes electronic configurations up to $3s10f$ with 90 terms, while the first 54 terms were adjusted to the energy levels given by the *NIST* database. The electronic configuration selected allowed us to compute the Υ_{ij} for the first 54 terms. However, the computation of transitions involving higher-lying terms could be considered in a future work since it would only signify considering a larger electronic structure and, hence, more time-consuming calculations.

The present improvements in the electron impact data are summarized in Table 1. The Υ_{ij} data considered initially for models 1401 and 1401a were obtained using SEA&VRM semi-empirical models for allowed and forbidden transitions, respectively. Two significant improvements were made to the new model regarding the Υ_{ij} data. First, the latest convergent close-coupling (CCC) data by Barklem et al. (2017) were included in the atomic model for the first 25 lower-lying terms, while the remaining values of SEA&VRM for higher levels were maintained. This combination is included in model 1401b. Then, in model 1401c, we further included perturbation distorted method calculations for transitions between levels 26 ($3s5g\,^1G$, 57 262.76 cm^{-1}) and 54 ($3s7i\,^1I$, 59 430.517 cm^{-1}), while the remaining values of SEA&VRM for higher levels and superlevels (55 | 59 649.15 cm^{-1} to 85 | 68 275 cm^{-1}) were maintained.

A qualitative comparison of the effective collision strength data sets considered in this work is presented in Fig. 5. The figure shows the comparison of the Υ_{ij} values at $T = 6000$ K given by the semi-empirical models considered (left panel) and the perturbation distorted wave calculations (right panel) with respect to the benchmark data (CCC) for the first 25 levels. The data sets from the semi-empirical model by SEA give a poor description for small and large transitions, while the VRM model is even worse, tending to underestimate the CCC values by several orders of magnitude with an opposite trend to the benchmark ones. The use of VRM formula has proven to be a generally bad approximation for the electron impact excitation cross sections (Sampson & Zhang 1992). On the other hand, as expected, the perturbation calculations are systematically larger than the CCC results by a factor of 5. The ratio Υ/Υ_{CCC} for the perturbation method presents a log-normal distribution, and the corresponding statistical parameters for all the approximations are shown in

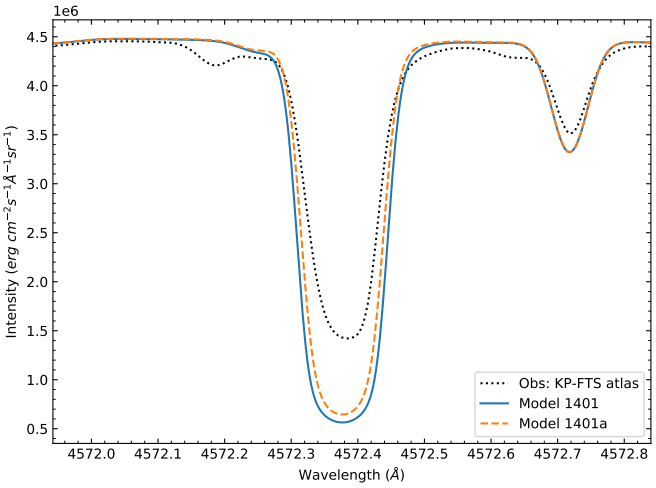

Fig. 6. Models 1401 (blue line) and 1401a (orange dashed line) compared to Kitt Peak Solar Atlas (KP-FTS) (Hase et al. 2010) intensity observations (black dotted line). Transition 4 572.4 Å shows a small improvement due to an update to the oscillator strength parameter, whose value decreased by 41%.

Table 2. Inspecting the DW and the semi-empirical values from model 1401c, we found that the results employed follow a similar statistical behavior.

4. Observations

The *SRPM* system produces a synthetic spectrum with an infinite spectral resolution that needs to be reduced to match the observed resolution data. To this end, the synthetic spectrum was convolved with a Gaussian function using a resolving power that depends on the resolution of observations used for comparison. In order to fairly judge the quality of the model and to take advantage of the information provided by the synthetic spectra, observations of mid to high resolution are required. The best solar observations we could obtain for each spectral range are described below.

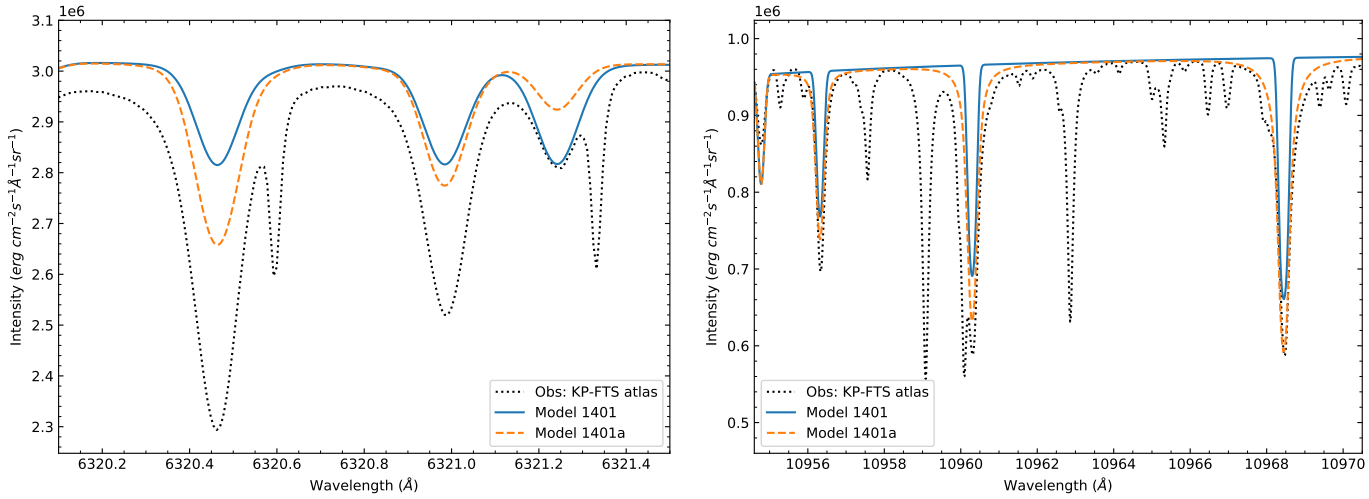

Fig. 7. Models 1401 (blue line) and 1401a (orange dashed line) compared to Kitt Peak Solar Atlas (KP-FTS) (Hase et al. 2010) intensity observations (black dashed line). Triplet transition around 6320 Å (*left panel*) shows improvements due to the update to the oscillator strength parameters, and the 10 964.38 Å profile (*right panel*) shows improvements due to changes in the broadening data (not included in model 1401).

Near-UV (NUV) range. Solar observations spanning a wide range in the NUV, not only in specific spectral lines such as the ones observed by the IRIS spacecraft, are not easy to find. We used irradiance data from 200 to 310 nm from Hall & Anderson (1991) (hereafter H&A). These observations were obtained from a stratospheric balloon that flew ~40 km in the stratosphere. Although these data are difficult to calibrate, because the UV Fraunhofer spectrum is extremely rich in absorption lines, H&A managed to combine and extrapolate it to zero optical depth to provide a reference spectrum with a spectral resolution of 0.01 nm.

Visible & Near-Infrared (NIR) ranges. In the range of 3290 to 12 510 Å, the selected observations were the Fourier-Transform-Spectra Solar Atlas (hereafter KP-FTS), obtained by Brault and coworkers at Kitt Peak Observatory (Neckel 1999), as described by Neckel & Labs (1984b,a) and Neckel (1994). According to Neckel (1999), the observations have no zero-point corrections to any of the FTS intensities; consequently, the absolute calibration for this disk-center ($\mu = 1$) spectrum is not reliable enough. For this reason, the calculated spectra were scaled (by adding a constant) to match the observed near continuum of the specific line profile under study.

Mid-Infrared (MIR) range. The data from ACE-FTS Solar Atlas[8] (Hase et al. 2010) were selected. The ACE-FTS is a space-borne Fourier transform spectrometer onboard the SCISAT-1 spacecraft. This Solar Atlas is a solar transmission spectrum recorded at altitudes above 160 km that covers the range of 22 500–130 000 Å, and it contains no atmospheric contribution. In the cited work, the authors mention that the spectral range was built from an average of 224 782 individual solar spectra, with a final 0.02 cm^{-1} resolution.

5. Results and discussion

After building the set of Mg I atomic models described in the previous sections, we ran the atmospheric models 1401a, 1401b, and 1401c using the *SRPM* system. We calculated the NLTE population for Mg I and all the other species present in the atmosphere. Once the converged populations was reached, we computed the synthetic spectra for each case.

The aim of this study is to identify the changes in line formation related to the distinctive atomic model used in calculating the spectra. To this end, we compared each new computed spectra with the synthetic spectra using the original model 1401 and solar observations in several spectral ranges. In this section, we report the results of this comparison and analyze which of the Mg I atomic model tested improves the match with the solar observations.

The information about the Mg I lines we used to compare with observations in this section is presented in Table 3. The last column in this table indicates the figure number where this transition is plotted. Several line profiles shown in the figures correspond to transitions between energy levels that had never been computed before in full NLTE.

5.1. Improvements owing to updated atomic data

We applied the updates described in Section 3.1 to model 1401a. The updated Einstein coefficients and broadening parameters produced noticeable changes, which improved the match with observations among the stellar spectra. Figures 6 and 7 show examples of this improvement. The first figure presents a comparison for a line profile calculated with models 1401 and 1401a and the Kitt Peak Solar Atlas. The computed line profile with model 1401a is slightly shallower than that calculated with model 1401, revealing the impact on the calculated line due to the updated oscillator strength, which decreased by 41%.

Both panels of Fig. 7 present triplet transitions, which are produced by a transition between different sublevels for the same upper and lower levels. The lines computed by model 1401a are deeper than those calculated using model 1401. In addition, each individual transition in the triplet calculated by 1401a has the correct change in depth following the observed lines, which is not present in the triplet obtained by 1401.

Calculated spectral lines in Fig. 7 (right panel) show the importance of considering a complete and accurate set of broadening parameters. In addition to the radiative damping, the Stark and van der Waals coefficients were also included in the atomic

[8] http://www.ace.uwaterloo.ca/solaratlas.php

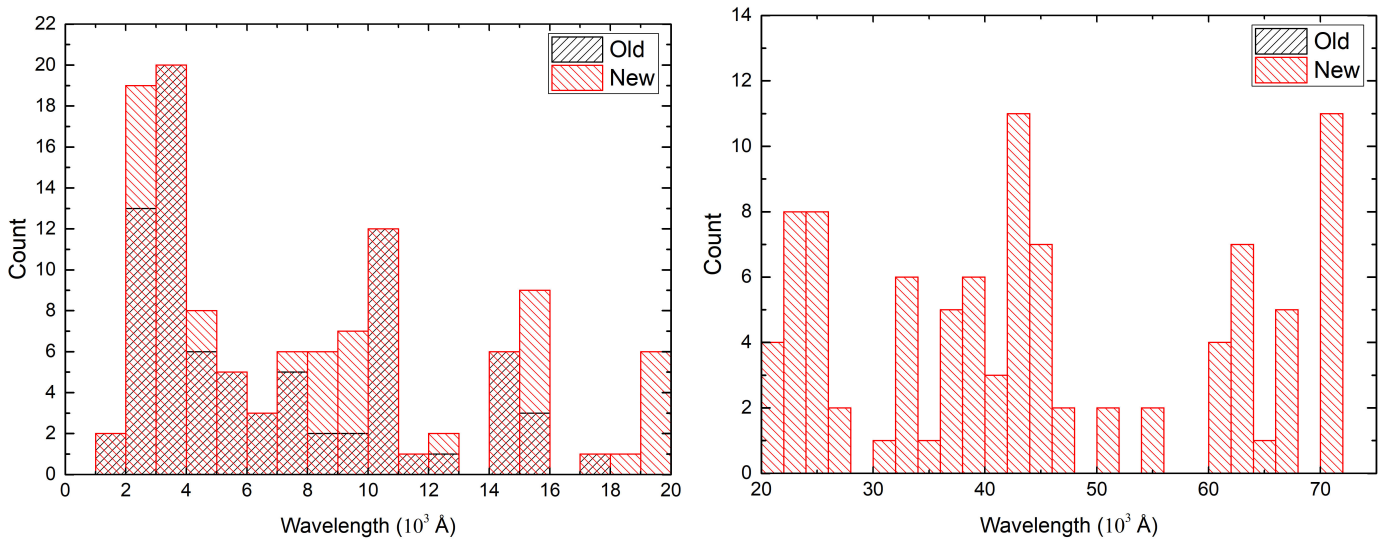

Fig. 8. Number of transitions included in the models. We note that 127 new lines were added. *Left*: Distribution of NUV to NIR lines for the 26-level (black) and 85-level (red) Mg I atomic models. *Right*: Distribution of new lines in the IR range. There are no lines beyond 18 000 Å in models of 26 energy levels.

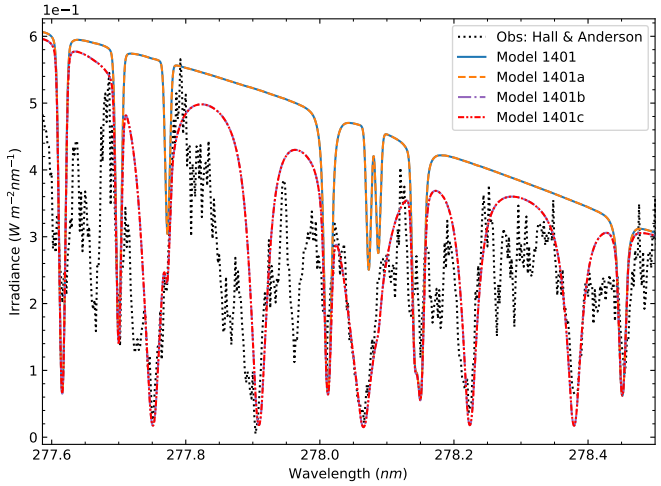

Fig. 9. NUV spectral lines. Models 1401 (blue line), 1401a (orange dashed line), 1401b (purple dashed-dotted line), and 1401c (red dashed-double-dotted line) vs. (H&A) solar irradiance observations (black dotted line). New transitions 2 780.65 Å are included in 85-level models 1401b and 1401c due to the incorporation of the $3p^2\,{}^3P$ term.

model of 1401a, producing wider wings that correctly match the KP-FTS Solar Atlas observations.

Regarding the Mg I density fraction, a small increase of 0.55% was found in model 1401a relative to model 1401. This means that the update made to the oscillator strength and to the Einstein coefficient have driven an overall population redistribution among Mg I, Mg II, and Mg III fractions. We note that 99.987% of this additional population of Mg I comes from Mg II and the rest from Mg III. Notwithstanding, the relative distribution of these ions presents the same behavior shown in Fig. 3.

5.2. Including more levels and lines

Models 1401 and 1401a use an atomic Mg I model of 26 energy levels. This allowed for only several transitions from the NUV to the NIR to be calculated, but this left aside other important transitions, especially in the IR. Examples of this limitation are shown in Figs. 9 and 11, where the transitions plotted in each panel are produced between levels not included in these models.

To solve this restriction, and in addition to the previously mentioned updates, we built two new models. Both 1401b and 1401c include an increased number of energy levels (detailed in Section 3.2) to reproduce new spectral lines across the studied range from NUV to MIR (1747–71 099 Å). Although these models consider the same number of energy levels, there is an important difference between them. In the next section, we address this topic. The number of spectral lines added to our database in each spectral range, together with the total number of lines considered in our models 1401b and 1401c, are listed in Table 4. The line distribution among the spectral range of interest is represented in Fig. 8.

In Fig. 9, the incorporation of the $3p^2\,{}^3P$ term allowed 1401b and 1401c models to reproduce the NUV lines shown in this plot. The match between the two calculated spectra (which are overlapped in the plot) and the H&A solar irradiance observations is remarkable. It is important to note that lines calculated using models with the same number of levels overlap, indicating that the change shown between calculated lines is triggered by only the number of levels considered.

The inclusion of more energy levels results in a general improvement to the calculated spectra. It permitted us not only to reproduce new spectral features but, in addition, it improved the

Table 4. Number of new and total lines in our models 1401b and 1401c.

Spectral Range (Å)	# New Lines	# Total Lines
FUV (100–2000)	0	2
NUV (2000–4000)	6	39
VIS (4000–7000)	2	16
NIR (7000–25 000)	39	73
MIR (25 000–71 100)	80	80

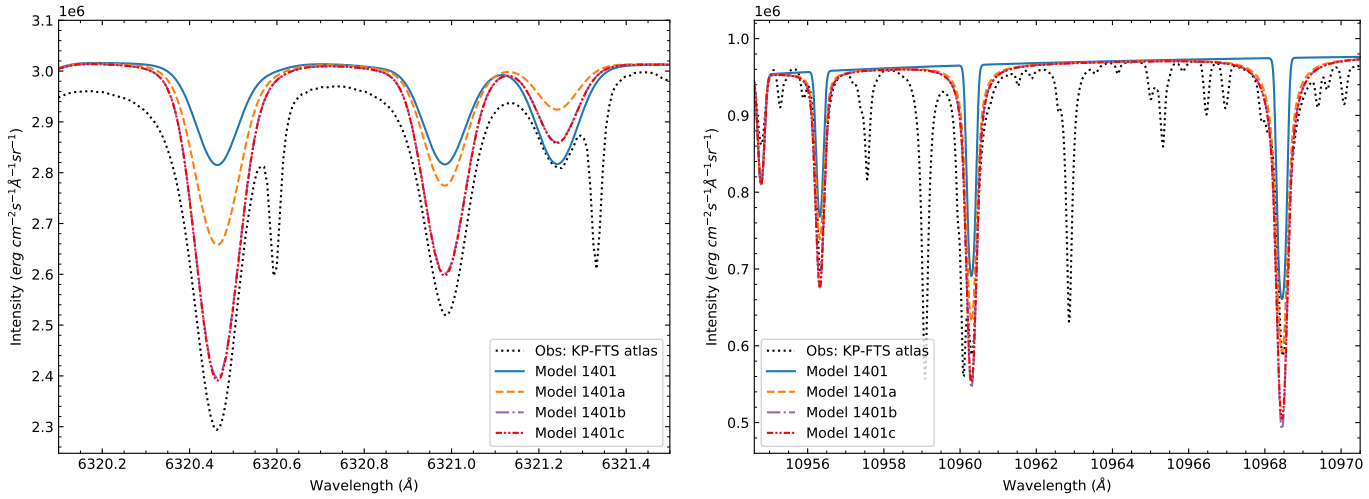

Fig. 10. VIS and NIR spectral lines. Models 1401 (blue line), 1401a (orange dashed line), 1401b (purple dashed-dotted line), and 1401c (red dashed-double-dotted line) vs. observations (black dotted line). *Left.* Visible range: transitions 6 320.72 Å compared to Kitt Peak Solar Atlas (KP-FTS) (Hase et al. 2010) intensity observations. Changes due to a higher number of levels (models 1401b and 1401c) are clearly visible. *Right.* NIR range: transitions 10 964.38 Å show improvements due to changes in the broadening data (not included in model 1401) and the increment in the number of energy levels (models 1401b and 1401c).

match in transitions between levels that have been already computed using a 26-level atom. This is evident in Fig. 10, where the lines calculated using 85-level models have a remarkable improvement over the computed profiles with 26-level models.

From the IR spectral lines added to our calculation, we selected four spectral features to illustrate the results. Figure 11 shows the following transitions: (*a*) 33 200.6 Å, (*b*) 36 807.6 Å, (*c*) 38 664.9, 38 669.1, and 38 670.4 Å, and (*d*) 71 092.0 and 71 097.4 Å, compared with ACE-FTS Solar Atlas IR observations. The 1401 and 1401a models do not consider the line, and the calculated spectra follow the continuum, while the models 1401b and 1401c display an acceptable match with observations. Although both models 1401b and 1401c produce deeper spectral lines than observed, the atomic model 1401c generates shallower lines than 1401b, improving the match for all lines included in the studied range. The upgrade obtained using model 1401c in matching the observations is described in the next section.

As a consequence of adding more levels to the model, a redistribution of the population among the ionized states of Mg occurred throughout the atmosphere. Each model follows the general behavior we have already presented in Fig. 3. However, we found an increase of 2.82% and 2.93% of Mg I for models 1401b and 1401c, respectively, relative to model 1401a. This additional population mainly comes from Mg II (~99.82%) and the remaining is from Mg III (~0.18%). Compared with model 1401a, we obtained an increase of about 2.0% and 2.1% in the ground state of Mg I in models 1401b and 1401c, respectively. This extra population mainly comes from Mg II and Mg III ionized states and, to a lesser extent, from Mg I higher levels. This last contribution is shown in Figure 12, where a decrease in the population for levels higher than the first two is evident in both models.

We attribute this result to a greater number of energy levels very close to the continuum, intentionally included to allow a flow of population from higher ionized to low-lying states, as it was suggested by Osorio et al. (2015) and Carlsson (1992). The redistribution of the Mg population throughout Mg I levels itself, as among the fraction of ionized states Mg I, Mg II, and Mg III, leads to levels involved in a specific transition that could be more populated or depopulated, changing the resulting profile.

5.3. New set of Υ_{ij}

Models 1401b and 1401c differ in the effective collision strength (Υ_{ij}) data. As it was detailed in Section 3.3, model 1401c included new calculations using the DW method for a transition whose upper level is in the range between 26 (57 262.76 cm^{-1}) and 54 (59 430.517 cm^{-1}).

The method of calculating the Υ_{ij} values in both models also produced a redistribution of Mg I energy levels, and among the ionized species Mg I, Mg II, and Mg III between them. However, these changes were more moderate than those found in the previous section. Figure 13 shows the ratio of the population of each level between models, integrated over all the atmospheric heights. The population of the first levels of model 1401c is higher than that of model 1401b. Although this behavior is similar to the one obtained in the previous section, the increase of the lower-lying level populations due to the DW Υ_{ij} data is one order of magnitude smaller.

The overall results in the calculated spectra, obtained with this significant change in Υ_{ij} data, could be separated into various distinctive regions. For transitions within 1747 Å and 12 510 Å, we have not found noticeable differences driven by it; although, at the end of this region, a small change begins to emerge. Figure 10 illustrates these findings since the calculated spectral lines from models 1401b and 1401c are superposed in each case. In these examples, and across the mentioned range, models of 85 levels (1401b and 1401c) produce almost identical line profiles, indicating that e+Mg I collisions have not played an important role in the line formation. It was not possible to find solar observations to compare from 12 510 to 22 500 Å, although the calculated spectra from both models presented an almost negligible difference of around 2 to 4% in some lines. The same pattern was observed until approximately 30 000 Å. MIR lines with wavelengths higher than that value were more sensitive to changes in Υ_{ij} data. We found differences larger than 6% at the center of several lines.

Figure 11 shows several examples in which model 1401b produced deeper lines than model 1401c. Although synthetic lines are still deeper than observations in both cases, the CCC

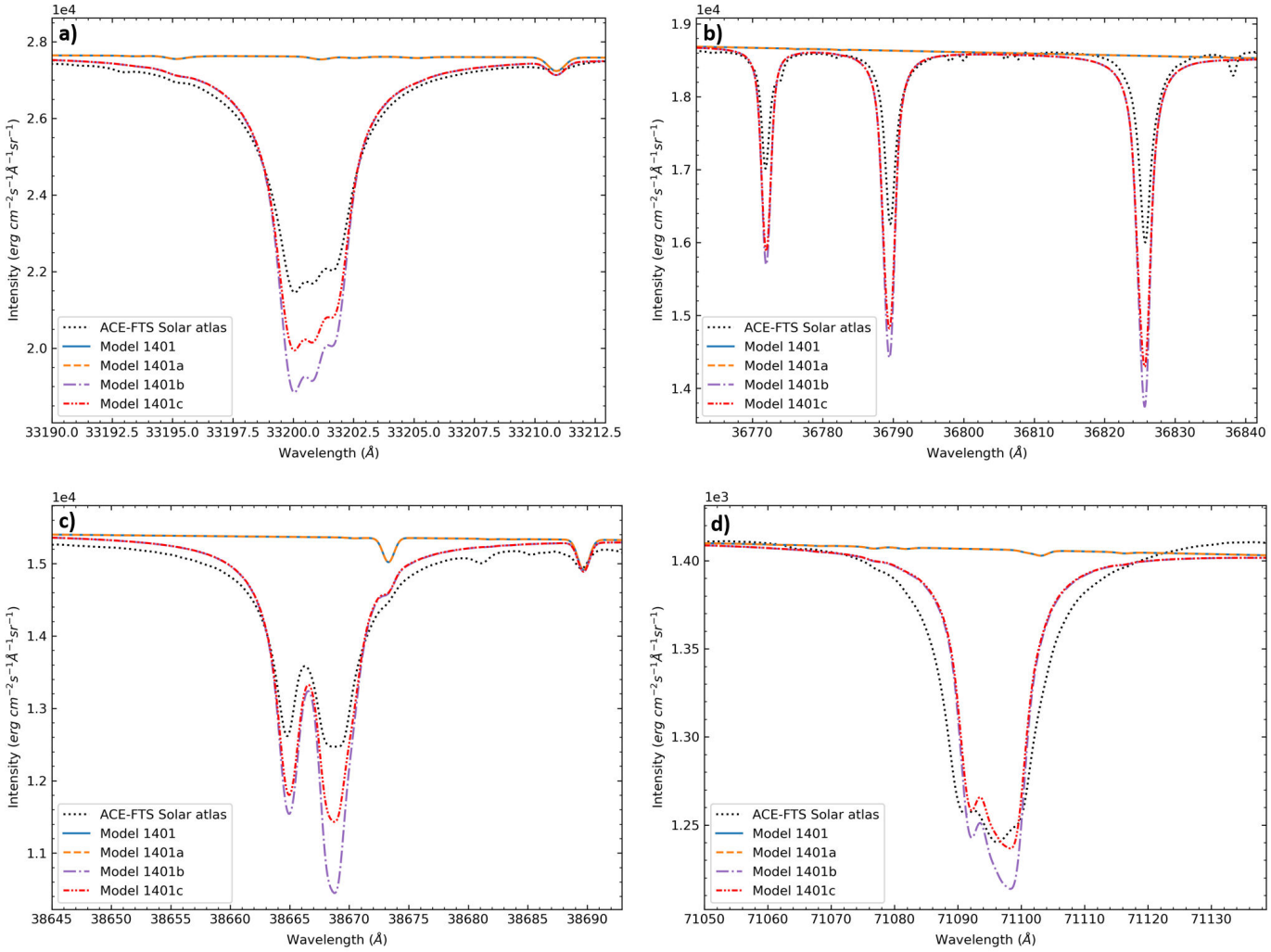

Fig. 11. IR computed spectral lines vs. ACE-FTS Solar Atlas observations (black dottedline). The 26-level models 1401 (blue line) and 1401a (orange dashed line) follow the continuum, and 85-level models 1401b (purple dashed-dotted line) and 1401c (red dashed-double-dotted line) fit the observations. Term-term transitions: (*a*) 33 200.6 Å, (*b*) 36 807.6 Å, (*c*) 38 664.9, 38 669.1, and 38 670.4 Å, and (*d*) 71 092.0 and 71 097.4 Å. See Table 3 for line parameters. Although synthetic lines are deeper than observations, Mg I model 1401c with the new DW Υ_{ij} data produces a better match throughout part of the IR range.

+ DW + SEA&VRM combination for Υ_{ij} (model 1401c) produced an important improvement in matching the observations throughout the IR range considered. In this spectral range, we found two kinds of improvement in the calculated spectra with 1401c over 1401b. On one side, there was a better match with observations in all the transitions with new DW Υ_{ij} data. On the other side, we also found an improvement in transitions involving the first 25 levels with the same Υ_{ij} in both models.

To analyze the effect in line formation caused by the different sets of Υ_{ij} data used in the calculation, we selected three lines to use as proxies for the changes observed in the calculated spectra. These lines are as follows: the insensitive NUV feature at 2 780.6 Å (shown in Fig. 9) and the improved MIR features 33 200 Å and 71 097 Å (shown in Figs. 11c and 11d, respectively). We computed the formation region of these lines in the atmosphere, using the contribution function (or attenuated emissivity; Fontenla et al. (2007)). Atmospheric parameters such as the temperature, pressure, and density at the formation height give information about the conditions of the plasma in which the NLTE populations and the emerging line profile were calculated.

Figures 14a and 14c present the contribution functions for the transitions that form the features 2 780.6 Å and 71 097 Å, respectively. The plot for 33 200 Å is not shown because it is very similar to 71 097 Å.

The center of the 2 780.6 Å feature formed in two distinctive regions. The former was located near the temperature minimum region at the end of the photosphere. And the other was located, at the beginning of the chromospheric plateau (see the atmospheric regions in Fig. 1). The peaks of the contribution function were at 666 km and 737 km, and around 1000 km, respectively. This wide range of heights in the atmosphere corresponds to temperatures between ~4000 to 6000 K.

The formation region was within ~175–390 km for the 71 097 Å feature. The maximum was located in the middle of the photosphere at 250 km, with temperatures from ~4500 to 5000 K. The 33 200 Å feature was produced within the same range, from 180 to 280 km. Both lines formed in a narrower temperature range and deeper in the atmosphere than the 2 780.6 Å feature. These examples illustrate spectral features that formed at different heights, where the atmospheric conditions in each case

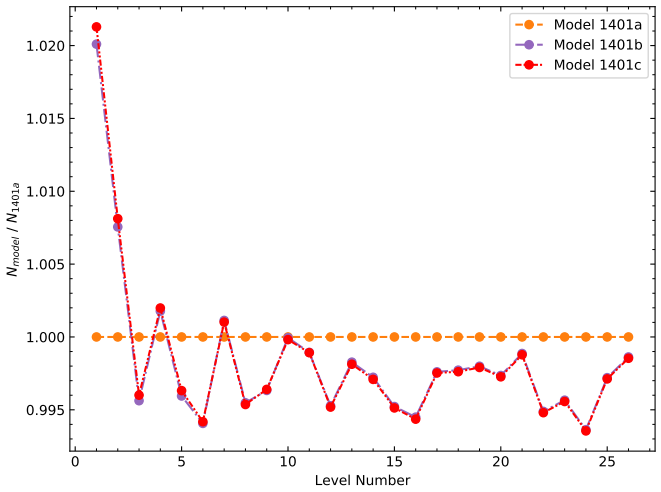

Fig. 12. Level population ratio for model 1401b (purple connected dots) and 1401c (red connected dots) with model 1401 (orange connected dots). For each level, a sum over all heights in the atmosphere was performed.

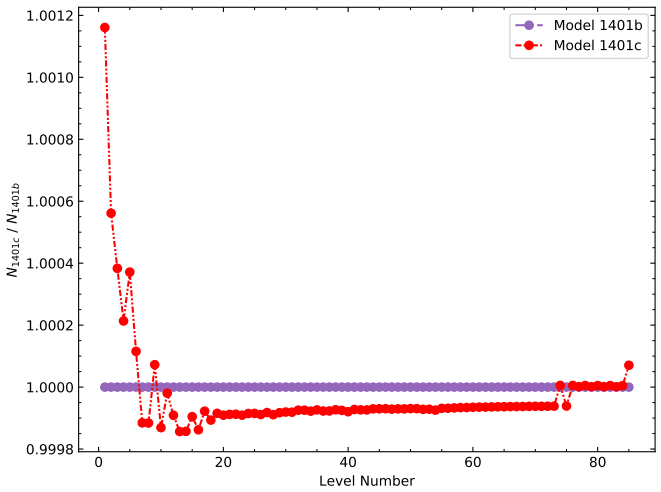

Fig. 13. Level population ratio between models 1401c and 1401b. For each level, a sum over all heights in the atmosphere was performed.

could constrain the physical processes that populate the energy levels involved. Our results suggest that lines that form in low-density atmospheric regions could be less affected by changes in the data that describe collisions with electrons.

Figure 14b shows a comparison of the Υ_{ij} parameters used in the 1401b and 1401c models for the line 2 780.6 Å at the temperature of the formation region. The Υ_{ij} value used at a specific temperature was obtained interpolating these data and then used to compute the NLTE population. Although the Υ_{ij} calculated using the DW method (adopted in model 1401c) is, on average, eight times higher than the values computed using the SEA&VRM method (adopted in model 1401b), the synthetic spectral feature calculated for each model remained unchanged (see in Fig. 9).

Instead, the 71 097 Å feature formed at photospheric heights, where the density of Mg I is more than two orders of magnitude higher than in the chromospheric plateau. Figure 14d shows that the Υ_{ij} data calculated using the DW method are about three times higher than for those computed using the SEA&VRM method. In this case, collisions with an electron appear to be more relevant since a remarkable improvement in matching the ACE Solar Atlas spectral lines was reached using the 1401c model, compared with that computed using 1401b model (see Fig. 11d).

The 33 200 Å feature is formed by a transition between levels 13 (54 192.256 cm^{-1}) and 24 (57 204.228 cm^{-1}), with CCC Υ_{ij} data in both models. This fact indicates that we had to find another way to study the influence of the Υ_{ij} values over the spectral line formation that takes the coupled system into account.

As the depth of a spectral line is related to the difference in the population of the levels involved, our results point out that there was a change among the energy level population distribution of Mg I due to the inclusion of DW calculations replacing SEA&VRM data. It provides an alternative way to analyze the influence of the Υ_{ij} on the calculated line. We used the level population ratio calculated as N_{low}/N_{up}, where N_{low} or N_{up} refers to the populations of each level involved in the transition at the formation height. This ratio allowed us to detect changes in the level populations that could be enough to affect the depth of the related spectral line.

Figure 15 presents the level population ratio for transitions 2 780.6 Å and 71 097 Å. The transition 2 780.6 Å produced an almost identical result for both 1401b and 1401c models, as we expected. This result again illustrates that even when changes in the Υ_{ij} data (shown in Fig. 14b) could be large, this has no influence on the level population ratio or the spectral line. A collisional process could not be the dominant process for this transition. Regarding the 71 097 Å feature in which the collisional process may play an important role (Fig. 14d), the level population ratio is different for each model as we predicted, being higher for model 1401b than 1401c.

Figure 16 shows the level population ratio for the 33 200 Å feature. Although the Υ_{ij} for this profile is the same as in data calculated with the CCC method in both models, it behaved similar to the ratio of level populations for the 71 097 Å profile.

To analyze the redistribution of the population among energy levels at the formation height, we computed the model population ratio (N_{1401c}/N_{1401b}) for the 85 energy levels at several heights in the atmosphere. In the height range from ~175 to 550 km, the population of model 1401c is larger than model 1401b for levels higher than level 20 ($5d\,^1D$, 56 308.381 cm^{-1}). This ratio reaches a maximum of about 12% at 350 km. Figure 17 shows the model population ratio at two representative formation heights, for feature 2 780.6 Å at 666.1 km, and features 71 097 Å and 33 200 Å at approximately 250 km.

Fig. 17 shows that at 250 km in the photosphere, the model population ratio for the first levels are slightly lower than 1. The population of model 1401c is redistributed to levels higher than ~20, where the model population ratio is bigger than unity by ~7%. The reason for this redistribution is due to the DW Υ_{ij} being larger than SEA&VRM Υ_{ij} data. The system is coupled through the statistical equilibrium equations, responding as a whole to the change in Υ_{ij} collisional parameters. The population of each level is affected by the rest of the levels present in the atomic model.

Regarding our proxy features, the 2 780.6 Å profile is formed by transitions from level 2 (21 850.405 cm^{-1}) to 28 (57 812.77 cm^{-1}) at 666.1 km. The model population ratio for both levels is close to 1, resulting in almost identical line profiles for models 1401b and 1401c at a formation height, as Fig. 9 indicates.

In the case of the 71 097 Å feature, the model population ratio for the levels involved (24 | 57 204.228 cm^{-1} and 38 |

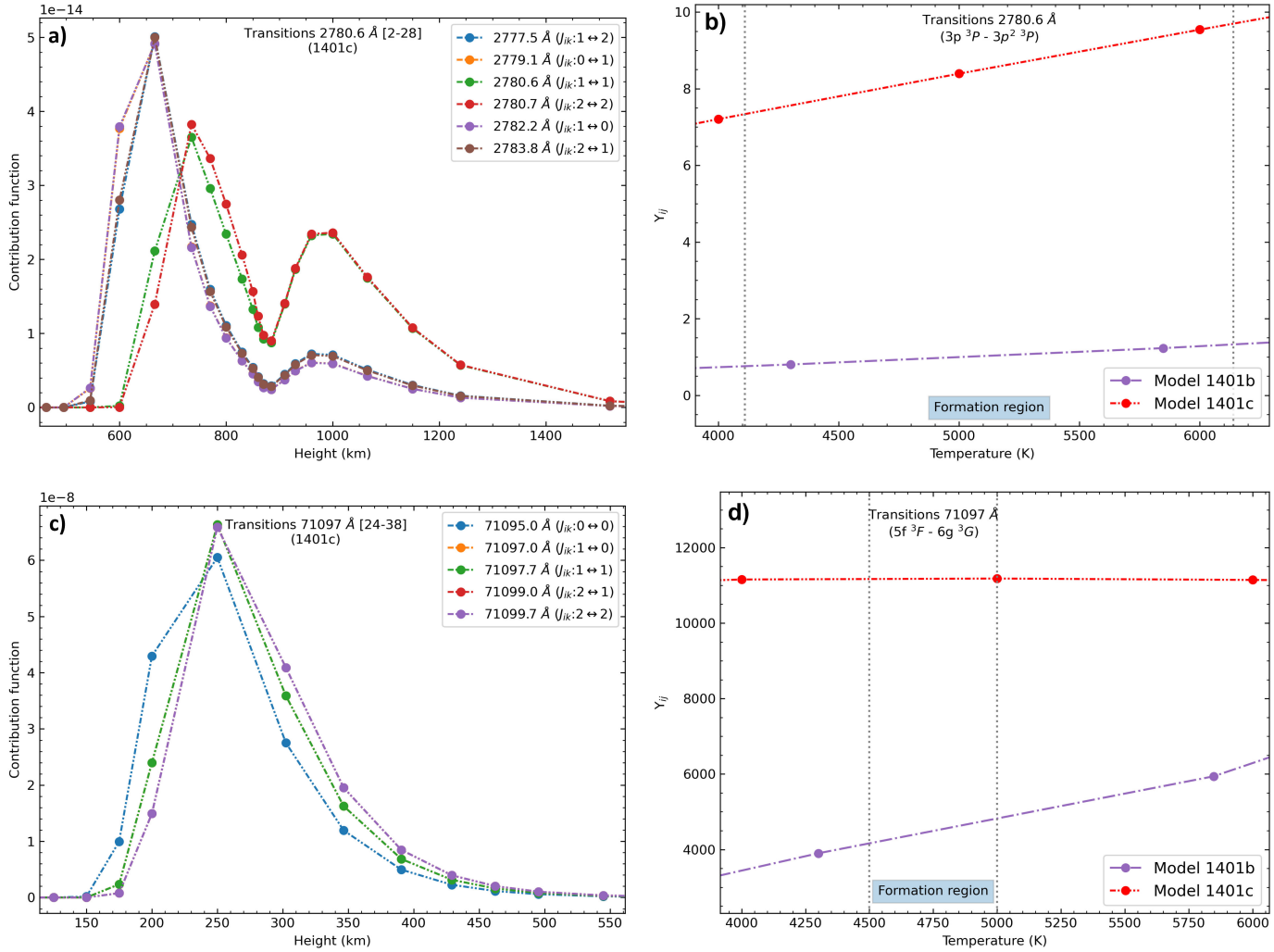

Fig. 14. *Left panel (Figs. (a) and (c))*: 1401c model contribution functions through the atmospheric height for lines involved in transitions 2 780.6 Å (a) and 71 097 Å (c). *Right panel (Figs. (b) and (d))*: Effective collision strength (Υ_{ij}) data at the formation region temperatures that were used to compute the populations for 2780.6 Å (b) and 71 097 Å (d) transitions in models 1401b (purple dashed-dotted line) and 1401c (red dashed-double-dotted line). The Υ_{ij} data provided by the DW method are greater than the SEA&VRM for all the transitions studied.

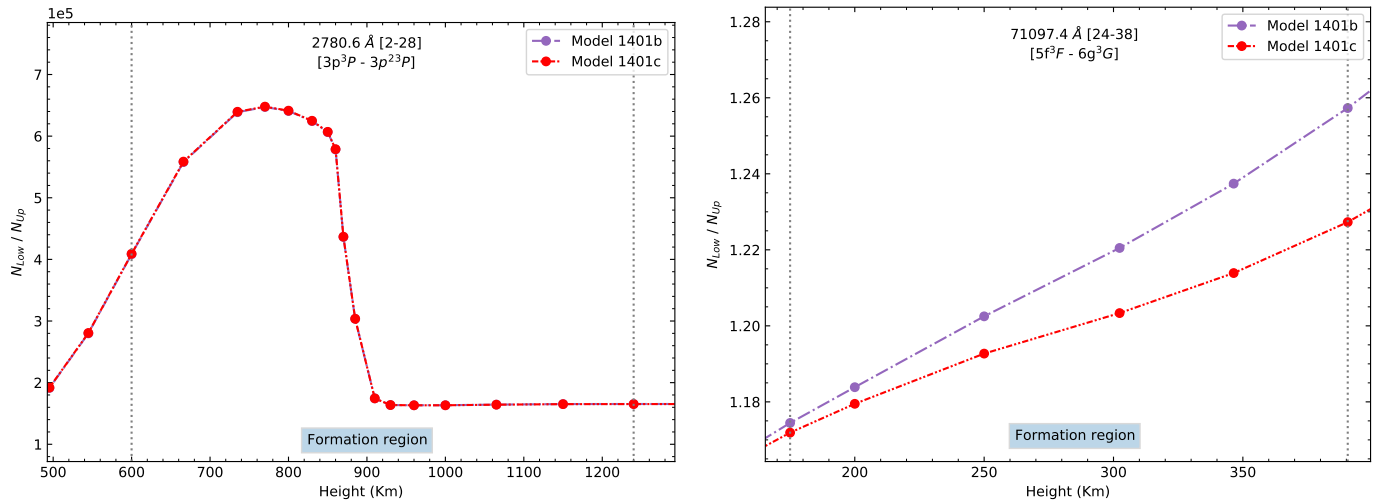

Fig. 15. Level Population ratio (N_{low}/N_{up}) at formation heights for transitions 2 780.6 Å (left) and 71 097 Å (right), following the examples in Fig. 14(a–b) and Fig. 14(c–d), respectively. *Left panel:* The ratios are identical for models 1401b (purple dashed-dotted line) and 1401c (red dashed-double-dotted line), producing the same line (shown in Fig. 9). *Right panel:* As in almost every IR transition, level population ratios are higher in model 1401b, producing deeper spectral lines (the line for this example is shown in Fig. 11d).

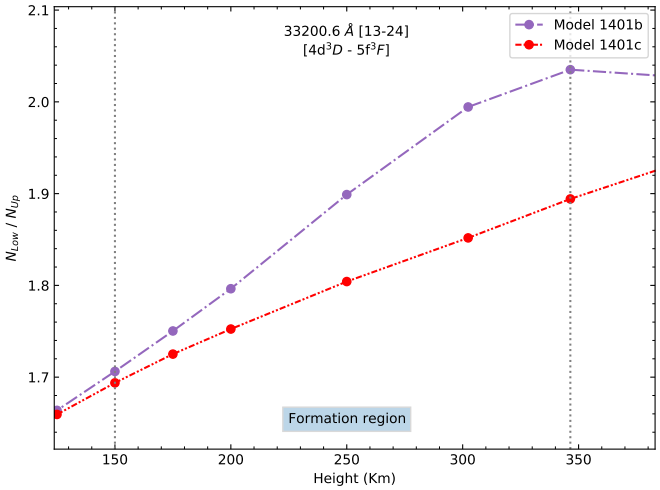

Fig. 16. Level population ratio for the 33 200.6 Å feature. Although both models used the same CCC Υ_{ij} data for the levels involved in the transition, the ratio changed due to the coupling with the rest of the levels in the atomic model.

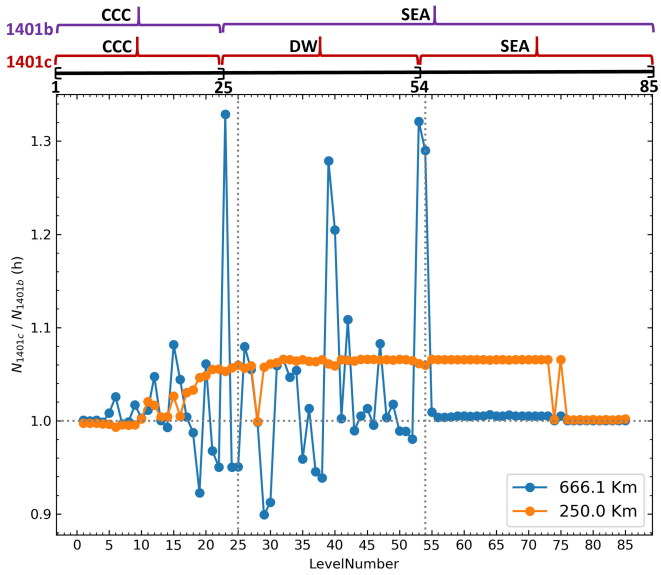

Fig. 17. Model population ratio as a function of the energy level at 250 km (orange connected dots) and 666.1 km (blue connected dots) in the atmosphere. In the top of the figure, the Υ_{ij} data used in each model are marked. The upper level determine the Υ_{ij} data used. For example, for transition 24–38 (71 097 Å), the SEA&VRM data were used in model 1401b (in purple) and DW data were used in model 1401c (in red).

59 430.517 cm^{-1}) at 250 km departs from unity by ~6% and ~7% respectively, as shown in Fig. 17. This small difference of ~1% at the formation height is responsible for the change on the calculated line profile between models.

The 33 200 Å feature is a transition between levels 13 (54 192.256 cm^{-1}) and 24 (57 204.228 cm^{-1}) at 250 km. The upper level involved in this transition has a higher population in model 1401c than in model 1401b, while the lower level has approximated the same population in both models. The extra Mg I population of level 24 in model 1401c could come from higher levels whose DW Υ_{ij} are higher than that of SEA&VRM in model 1401b. Although the numerical value of the Υ_{ij} in this specific transition is the same in both models, the population changes are due to the value of Υ_{ij} of the rest of the levels.

In general, when the model population ratio at the formation height for each level involved in a transition is unity, then the transition has the same line profile in the calculated spectra for both models. On the contrary, if the model population ratio of the lower level is less than that of the upper level, then the line profile is shallower in model 1401c. As Fig. 17 indicates, all line profiles with a formation height of ~250 km (where most of the MIR line formed) whose lower level is approximately less than ~20 and the upper level is bigger than ~20, except for level 28 (57 812.77 cm^{-1}), are shallower in model 1401c, improving the match with solar observations.

One significant Mg I feature in the NUV range is the resonance 2852 Å line profile resulting from the transition between levels 1 and 3 (35 051.264 cm^{-1}). This profile could be used as an important diagnostic of the thermal structure in solar or stellar chromospheres. Figure 18 shows a comparison of the H&A solar irradiance observations with the synthetic line calculated with models 1401, 1401a, 1401b, and 1401c. The calculated profiles are slightly sensitive to an increase in the number of levels since 1401 overlaps with 1401a. The same behavior occurs with 1401b and 1401c, although in this case the center of the line is almost negligibly shallower and the upper part of the wings are lower than the other models.

Fontenla et al. (2016) and Tilipman et al. (2021) built atmospheric models for the dM stars GJ 832 and GJ 581 using the stellar version of the *SRPM*. These stellar models were calculated with our initial Mg I atomic model (1401). The NUV synthetic spectra computed in these works revealed an incorrect emission in the center of the 2852 Å line, in comparison with STIS G230L *HST* observations. In a forthcoming paper, we will address this problem, testing our new Mg I atomic model 1401c, given the different plasma characteristics of the atmosphere of stars cooler than our Sun.

6. Conclusions

The selected data of the Mg I atomic model used in solving the NLTE population and calculating the spectra are crucial factors to improve the agreement of Mg I line profiles in solar observations from NUV to MIR. Updates in the oscillator strengths and the broadening parameter describing radiative, Stark, and van der Waals processes produced noticeable changes in the calculated line profiles. Our model 1401a showed a clear improvement over the initial model 1401, driven by a redistribution of the Mg population among its ionization states and mainly throughout the Mg I atomic levels themselves.

To reach our goal of including important features of Mg I from the NUV to the MIR spectral range, we developed a new level structure shown by the Grotrian diagram of Fig. 4 for the models 1401b and 1401c. Starting from a simple atomic structure of 26 levels, we ended with a robust structure of 85 levels capable of reproducing a long list of transitions, many of which have never been calculated in NLTE and studied in detail before.

Regarding the effective collision strength Υ_{ij} parameter, we made use of the latest CCC calculation by Barklem et al. (2017) for the first 25 levels. For the following levels, we considered the widely used formulation of SEA&VRM (yielding the model 1401b). To find a better agreement in the line profiles, we performed a new calculation for these parameters from levels 26 (57 262.76 cm^{-1}) to 54 (59 430.517 cm^{-1}) with the multiconfiguration Breit–Pauli distorted–wave (DW) method (used by

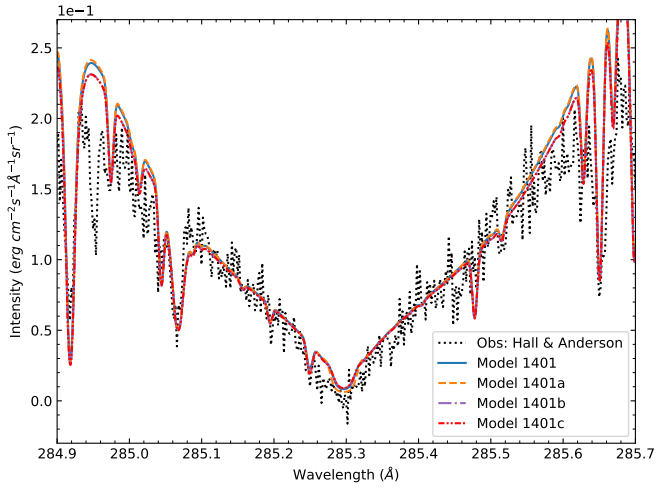

Fig. 18. Comparison of the H&A solar irradiance observations of the 2852 Å line profile with the synthetic line calculated from models 1401, 1401a, 1401b, and 1401c.

model 1401c). This method has seldom been used in stellar astrophysics. We found an additional improvement to that obtained updating and expanding the level structure due to the DW Υ_{ij} calculation. The synthetic spectra obtained using the model 1401c reached a better agreement with solar observations from NUV to MIR (1747–71 099 Å) than the other models considered. Nevertheless, the observed profiles are still shallower than the calculated lines.

These results open new challenges for future work. We will continue to improve the calculation of the Υ_{ij} data from level 55 to 85 using the DW method. The inclusion of these new data in the statistical equilibrium equations could produce a redistribution of the Mg population similar to that obtained in the present work. It could imply even shallower line profiles than those obtained with the model 1401c, potentially achieving an excellent match with solar observations.

The DW method has shown to be a better alternative to SEA&VRM for calculating the Υ_{ij} parameters of Mg I when close-coupling methods are impracticable or data are not available. We suggest that its application to other atomic species should be a more reliable option to semi-empirical calculations.

As the effective collision strength parameters depend on the temperature, the plasma characteristics of the region in which a transition is formed determine the NLTE population and the resulting line profile. Forthcoming work will mainly cover the NLTE Mg I line formation in stars with different spectral types, with a special interest in stars cooler than our Sun with planets in its habitable zone.

Acknowledgements. We wish to sincerely thank to Dr. Jeffrey Linsky for his detailed revision of our manuscript since it has helped us improve our work. This work has made use of the *VALD* database, operated at Uppsala University, the Institute of Astronomy RAS in Moscow, and the University of Vienna. We acknowledge to 1995 Atomic Line Data (R.L. Kurucz and B. Bell) Kurucz CD-ROM No. 23. Cambridge, Mass.: Smithsonian Astrophysical Observatory.

References

Alexeeva, S., Ryabchikova, T., Mashonkina, L., & Hu, S. 2018, ApJ, 866, 153
Badnell, N. R. 2011, Computer Physics Communications, 182, 1528
Barklem, P. S., Osorio, Y., Fursa, D. V., et al. 2017, A&A, 606, A11
Bergemann, M., Kudritzki, R.-P., Gazak, Z., Davies, B., & Plez, B. 2015, ApJ, 804, 113
Butler, K. & Giddings, J. 1985, Newsletter on the analysis of astronomical spectra, University of London, 9, 9
Carlsson, M. 1992, in Astronomical Society of the Pacific Conference Series, Vol. 26, Cool Stars, Stellar Systems, and the Sun, ed. M. S. Giampapa & J. A. Bookbinder, 499
Cunto, W., Mendoza, C., Ochsenbein, F., & Zeippen, C. J. 1993, A&A, 275, L5
Fontenla, J. & Harder, G. 2005, Mem. Soc. Astron. Italiana, 76, 826
Fontenla, J. M., Avrett, E., Thuillier, G., & Harder, J. 2006, ApJ, 639, 441
Fontenla, J. M., Avrett, E. H., & Loeser, R. 1990, ApJ, 355, 700
Fontenla, J. M., Avrett, E. H., & Loeser, R. 1991, ApJ, 377, 712
Fontenla, J. M., Balasubramaniam, K. S., & Harder, J. 2007, ApJ, 667, 1243
Fontenla, J. M. & Landi, E. 2018, ApJ, 861, 120
Fontenla, J. M., Linsky, J. L., Witbrod, J., et al. 2016, arXiv e-prints, arXiv:1608.00934
Fontenla, J. M. & Rovira, M. 1985, Sol. Phys., 96, 53
Fontenla, J. M., Rovira, M., Vial, J. C., & Gouttebroze, P. 1996, ApJ, 466, 496
Fontenla, J. M., Stancil, P. C., & Landi, E. 2015, ApJ, 809, 157
Hall, L. A. & Anderson, G. P. 1991, J. Geophys. Res., 96, 12,927
Hase, F., Wallace, L., McLeod, S., Harrison, J., & Bernath, P. 2010, Journal of Quantitative Spectroscopy and Radiative Transfer, 111, 111
Kramida, A., Yu. Ralchenko, Reader, J., & and NIST ASD Team. 2004, NIST Atomic Spectra Database (ver. 3.0.beta), [Online]. Available: `https://physics.nist.gov/asd` [2004]. National Institute of Standards and Technology, Gaithersburg, MD.
Kramida, A., Yu. Ralchenko, Reader, J., & and NIST ASD Team. 2020, NIST Atomic Spectra Database (ver. 5.7.1), [Online]. Available: `https://physics.nist.gov/asd` [2020, October 27]. National Institute of Standards and Technology, Gaithersburg, MD.
Kupka, F. G., Ryabchikova, T. A., Piskunov, N. E., Stempels, H. C., & Weiss, W. W. 2000, Baltic Astronomy, 9, 590
Kurucz, R. L. & Bell, B. 1995, Atomic Line Data, Kurucz CD-ROM No. 23., www.cfa.harvard.edu/amp/ampdata/kurucz23/sekur.html, [Online; accessed: 2020, October 27]
Landi, E., Del Zanna, G., Young, P. R., Dere, K. P., & Mason, H. E. 2012, ApJ, 744, 99
Neckel, H. 1994, in Invited Papers from IAU Colloquium 143: The Sun as a Variable Star: Solar and Stellar Irradiance Variations, ed. J. M. Pap, C. Frohlich, H. S. Hudson, & S. K. Solanki, 37
Neckel, H. 1999, Sol. Phys., 184, 421
Neckel, H. & Labs, D. 1984a, Sol. Phys., 92, 391
Neckel, H. & Labs, D. 1984b, Sol. Phys., 90, 205
NRL Plasma Formulary, D. L. 2005, NRL (Naval Research Laboratory) plasma formulary, revised, Naval Research Lab. Report
Osorio, Y. & Barklem, P. S. 2016, A&A, 586, A120
Osorio, Y., Barklem, P. S., Lind, K., et al. 2015, A&A, 579, A53
Sampson, D. H. & Zhang, H. L. 1992, Phys. Rev. A, 45, 45
Scott, P., Grevesse, N., Asplund, M., et al. 2015, A&A, 573, A25
Seaton, M. J. 1962, Proceedings of the Physical Society, 79, 1105
Tilipman, D., Vieytes, M., Linsky, J. L., Buccino, A. P., & France, K. 2021, ApJ, 909, 61
van Regemorter, H. 1962, ApJ, 136, 906
Vieytes, M. C. & Fontenla, J. M. 2013, ApJ, 769, 103
Zhao, G., Butler, K., & Gehren, T. 1998, A&A, 333, 219
Zhao, G. & Gehren, T. 2000, A&A, 362, 1077